Phase diagram of magnetic nanodisks measured by scanning electron microscopy with polarization analysis

S.-H. Chung,[1,2] R. D. McMichael,[1] D. T. Pierce,[1] and J. Unguris[1]

[1]*Center for Nanoscale Science and Technology, NIST, Gaithersburg, Maryland 20899, USA*
[2]*Maryland NanoCenter, University of Maryland, College Park, Maryland 20742, USA*

We use scanning electron microscopy with polarization analysis (SEMPA) to image the magnetic domain structures of *individual* ferromagnetic nanodisks with different diameters and thicknesses, and thereby determine the phase diagram of the magnetic ground states in these technologically important magnetic structures. Depending on the nanodisk dimensions, we observe magnetic structures based on one of three configurations: a single-domain in-plane, a single-domain out-of-plane, or a vortex state. By imaging the in-plane and out-of-plane magnetization components of identically prepared $Ni_{80}Fe_{15}Mo_5$ nanodisks with diameters that range from 35 to 190 nm and with thicknesses that range from 10 to 65 nm, we are able to locate phase boundaries between the three different phases and the triple point. The phase boundaries are not sharply defined, however. Near the boundaries and especially near the triple point, we observe disks in a mixture of the different metastable ground phases, and we observe variations of the basic states, such as a tilted vortex configuration. A magnetic phase diagram generated by a micromagnetic simulation is found to be in good qualitative agreement with the phase diagram determined by the SEMPA measurements. The ability to determine the magnetic phases in sub-100 nm nanodisks enables tailoring material properties and geometry of nanodisks for various potential applications.

PACS number(s): 75.75.−c

I. INTRODUCTION

The behavior of magnetic nanostructures is technologically important for possible applications[1] such as magnetic data storage,[2] magnetic memory,[3] and spintronic devices.[4] In particular, magnetic nanodisks of soft ferromagnetic materials with sizes less than 100 nm are of recent interest due to their unique magnetic properties compared to micron size or bulk state ferromagnets. In the sub-100 nm size range, the energy cost to support domain walls and multidomain structures becomes prohibitive and the magnetization configuration of many magnetic materials favors a single-domain state. "Single domain" in this context does not necessarily mean uniform magnetization, however. Especially for soft magnetic materials, the magnetization typically has nonuniformities such as curling near surfaces and edges, due to nonuniform dipolar fields.[5–7]

Depending on the aspect ratio (thickness/diameter), the magnetic configuration of nanodisks with dimensions less than 100 nm is based on one of three ground states: a single-domain in-plane state, a single-domain out-of-plane state, or a vortex state as illustrated in Fig. 1.[8] Nanodisks with a low aspect ratio form single-domain in-plane states and nanodisks with a high aspect ratio form single-domain out-of-plane states. Nanodisks with an intermediate aspect ratio and diameter several times larger than the magnetic exchange

FIG. 1. Schematic illustration of the three basic nanodisk magnetic ground states: (a) in-plane state, (b) out-of-plane state, and (c) vortex state.

length $l_{ex} = \sqrt{2A/\mu_0 M_s^2}$ (A: exchange stiffness and M_s: the saturation magnetization) form in-plane flux closure states or magnetic vortex states. In the vortex state, the magnetization forms a flux-closed loop following the circumference of the disk, and turns toward the surface normal to either the top or bottom of the disk in the vortex core, which typically has a lateral size of a few times l_{ex}. Vortices are characterized by two parameters, chirality and polarity. Chirality is the sense of the in-plane flux closure and is either clockwise or counterclockwise. Chirality determines the direction of the vortex core motion under a dc magnetic field.[9] Polarity describes the magnetization direction at the center of the vortex, either into or out of the surface plane. The polarity determines the sense of dynamic vortex core gyration in the in-plane excitation mode.[10]

Determining the phase diagram of magnetic nanodisks is important since this enables one to tailor magnetic material properties and geometries for possible applications. For example, the single-domain in-plane state was used to demonstrate the room-temperature magnetic quantum cellular automata,[11] and the vortex state has been investigated for potential data storage by switching vortex core polarity.[12,13]

The ground-state magnetic phase diagram is determined by minimizing the total energy as a function of the nanodisk diameter and thickness. Neglecting the Zeeman energy, the total magnetic energy is given by the sum of the exchange energy, the magnetostatic energy, and the magnetocrystalline anisotropy energy,[14]

$$E_{tot} = \int_V \left\{ \frac{A}{M_s^2} \sum_{i=x,y,z} (\nabla M_i)^2 - \frac{\mu_0}{2} \overrightarrow{H_d} \cdot \overrightarrow{M_s} + f_k \right\} dV, \quad (1)$$

where A is the exchange stiffness, M_s is the saturation magnetization, H_d is the demagnetizing field, and f_k is the magnetocrystalline anisotropy energy density. The exchange in-
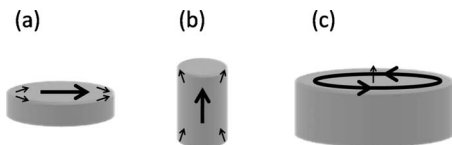
teraction favors parallel spin alignment whereas the magnetostatic interaction favors divergence-free spin alignment to reduce the total energy. The total magnetic energy landscape depends on the geometry and magnetic material properties of the nanodisks and contains both global and local energy minima. For a given geometry the global energy minimum determines the ground-state magnetic configuration among the possible stable magnetization configurations. However, local energy minima also play an important role since they can lead to nanodisks that are stabilized in metastable magnetic configurations.

Various micromagnetic simulations,[7,8,15] analytical methods,[16,17] and analytical scaling of micromagnetic simulations[18–20] have been used to model the magnetic behavior of ferromagnetic nanodisks, and to compute the phase diagram of magnetic ground states (i.e., global energy minimum state) as a function of the diameter and thickness of the nanodisks. The various phase diagrams from the different models and different material properties may be directly compared by expressing the results in terms of the reduced thickness, t/l_{ex}, and diameter, D/l_{ex}. Of course, comparing published results assumes that magnetocrystalline effects are small and care must be taken to ensure a consistent definition of l_{ex}. The resulting model phase diagrams have similar features. The phase boundary between the in-plane and out-of-plane states lies close to the boundary calculated for uniformly magnetized cylinders which corresponds to a constant aspect ratio of $t/D=0.9065$.[21] And the disk diameter at the triple point ranges between 6.8 and 8.3 exchange lengths. In addition, analytical methods have also been used to map regions of the phase diagram where metastable states may occur.[22]

Previous experimental measurements to determine the magnetic nanodisk phase diagram in the vicinity of the triple point were mostly based on the *average* properties of nanodisk arrays obtained from hysteresis curve measurements. Ross *et al.* used various magnetometry techniques to determine the magnetic state of samples prepared by electrodeposition into templates made by interference lithography.[8,23] Superconducting quantum interference device magnetometry was used to measure the magnetization of arrays deposited through nanoporous alumina shadow masks.[18] Magneto-optical magnetometry was used to determine the magnetic state of nanodisks patterned by electron-beam lithography[24] and nanoimprint lithography.[25] In general, these magnetometry measurements require a magnetization model to determine the magnetic structures from the magnetization curves. It is difficult to determine from these averaged measurements if multiple magnetic states are present. Furthermore, to provide sufficient signal, averaged measurements can require densely packed arrays that may be magnetostatically coupled.

Some direct imaging of the magnetic domain structure of individual nanodisks near the triple point has been accomplished using magnetic force microscopy (MFM) and various types of Lorentz electron microscopies. However, the previous MFM imaging studies could not determine the nanodisk phase diagram near the triple point since those measurements were often limited to *perpendicularly* magnetized nanodisks[23,26] or magnetic disks larger than 100 nm in
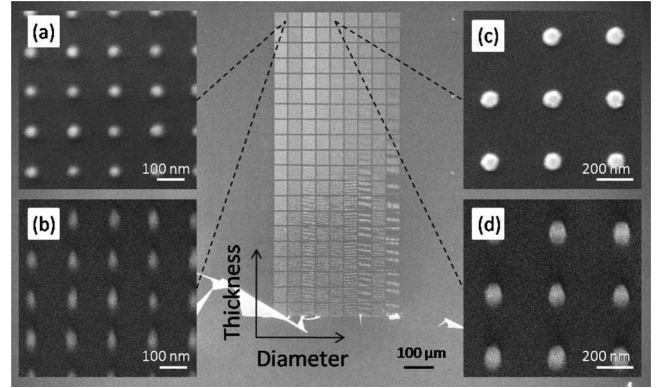

FIG. 2. SEM image showing a low magnification overview of the patterned sample with nanodisk arrays of nine different diameters and continuously varying thickness. The insets show high magnification images from two arrays acquired at two sample tilts: (a)/(b) 65 nm thick $\times 35$ nm diameter nanodisks and (c)/(d) 65 nm thick $\times 90$ nm diameter nanodisks. Sample tilt is 0° in (a)/(c) and 45° in (b)/(d).

diameter.[25] Lorentz and holographic transmission electron microscopy methods also provide an incomplete picture since they are limited to imaging magnetization components perpendicular to the electron beam,[27,28] and these studies have also focused on larger nanodisks.[29] Determining the phase diagram of magnetic nanodisks has been a challenge for magnetic microscopy since it requires a noninvasive measurement of both the in-plane and out-of-plane magnetization components with high resolution.

In this work, we systematically determine the shape-dependent phase diagram of sub-100 nm disks by measuring the three-dimensional magnetic structure of *individual* nanodisks using high-resolution scanning electron microscopy with polarization analysis (SEMPA). We observe magnetic configurations based on three distinct ground phases (single-domain in-plane, single-domain out-of-plane, and vortex states) depending on the diameters and thicknesses of the soft magnetic nanodisks. Near the phase boundaries and the triple point, we observe mixtures of different metastable ground phases. Near the boundaries we also observe variations of the basic phases, such as tilted vortex states. The magnetic phase diagram generated by using a micromagnetic simulation code agrees qualitatively with the SEMPA observations.

II. EXPERIMENT

To ensure that all of the nanodisks were prepared under the same conditions, a single sample with a range of thicknesses and diameters was prepared. Nanodisks of different diameters were defined using electron-beam lithography in polymethyl-methacrylate resist. The patterns were generated in an 0.5 mm $\times$ 1 mm electron-beam exposed area, which was subdivided into 50 μm $\times$ 50 μm regions each containing an array of nanodisks of a single diameter as seen in the SEM image in Fig. 2. A thin Ta film (3 nm) was used as a buffer layer on the Si substrate, and the polycrystalline $Ni_{80}Fe_{15}Mo_5$ (Ref. 30) wedge film was deposited in an

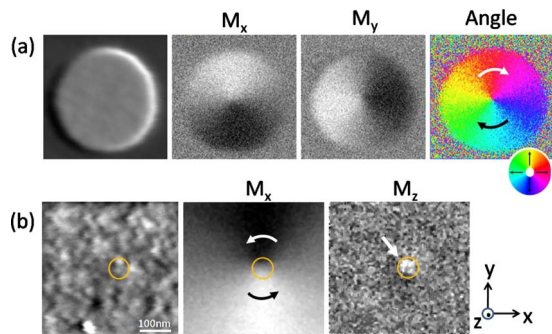FIG. 3. (Color online) Examples of SEMPA measurements from 1 μm diameter $\times$25-nm-thick permalloy disks. (a) Simultaneously measured images of the topography and the two in-plane (M_x and M_y) magnetization components, and the corresponding, derived in-plane magnetization direction. The magnetization direction is represented by the colors shown in the inset color wheel. (b) Simultaneously measured images of the topography, the in-plane (M_x) and the out-of-plane (M_z) magnetization components from the central region of a disk with opposite chirality. The vortex chirality and polarity can therefore be measured simultaneously.

electron-beam evaporation chamber under high-vacuum conditions (1.6×10^{-5} Pa). A linearly varying thickness wedge was generated by using a moving shadow mask during deposition. Lift-off of the unwanted film left behind an array of nanodisks with diameters that ranged from 35 to 190 nm and with thicknesses that ranged from 10 to 65 nm. The maximum thickness variation over each square region due to the shutter motion is ± 1.4 nm. The thickness was measured using a calibrated atomic force microscope. The array period was designed to be five times larger than the nanodisk diameter so that the magnetostatic interactions between nanodisks are negligible. High magnification SEM images such as those in the insets of Fig. 2 show that disk diameters were well defined and uniform even in the smallest disks; however the tallest pillarlike disks were slightly tapered [Figs. 2(b) and 2(d)].

SEMPA was used to directly image the in-plane and out-of-plane magnetic structure of the nanodisks. SEMPA measures the magnetization within a few nanometers of the surface by measuring the spin polarization of the emitted secondary electrons.[31,32] As the unpolarized incident electron beam from the field-emission SEM is rastered over the sample surface, the topographic image is derived from the secondary electron intensity while the magnetization image is simultaneously derived from the secondary electron-spin polarization, $P = (N_\uparrow - N_\downarrow)/(N_\uparrow + N_\downarrow)$, where $N_\uparrow(N_\downarrow)$ are the number of electrons with spins aligned (antialigned) with a particular measurement direction. Our spin-polarization analyzers can simultaneously measure either the two in-plane magnetization components (M_x and M_y) or one in-plane (M_x) and one out-of-plane (M_z) magnetization component. Examples of SEMPA measurements obtained from 1 μm diameter $\times$25-nm-thick permalloy disks are presented in Fig. 3. This disk diameter is somewhat larger than the ones used in this study but it is still in a single vortex state. The chirality of the vortex state in the disk of Fig. 3(a) is determined by calculating the in-plane magnetization direction from M_x and M_y images, which is represented by the angle image. In fact,
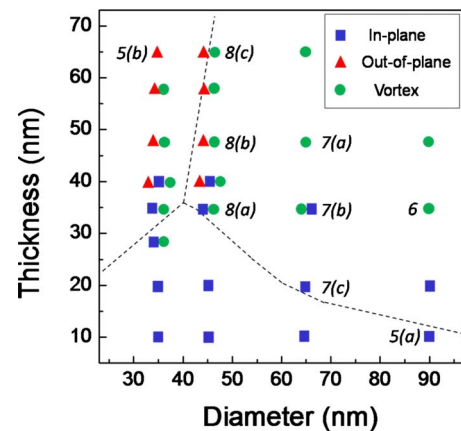

FIG. 4. (Color online) Summary of the magnetic states observed in SEMPA images as a function of disk size and shape. Disk diameters were either 35, 45, 65, or 90 nm. Near the phase boundaries, multiple grouped symbols indicated that multiple states were observed for the same disk diameter and thickness. The dashed lines are taken from the main phase boundaries calculated by the OOMMF micromagnetic simulations [see Fig. 9(a)]. The numbers next to the data points refer to corresponding figures in this paper.

the chirality can be determined by just one in-plane component. Figure 3(b) shows the topography, in-plane M_x and out-of-plane M_z images from a disk with opposite chirality. The dark region in the upper half and the bright region in the lower half of the M_x image in Fig. 3(b) shows that this disk has counterclockwise chirality. The M_z image shows a small white spot at the center of the vortex. This is a magnetic vortex core with positive polarity. SEMPA can simultaneously measure the chirality and polarity of the vortex. The diameter of the core is about 15 nm and is near the limit of SEMPA resolution. In comparison, the diameters of the smallest disks in this study are 35 nm so that disks with out-of-plane magnetization are clearly resolved.

III. RESULTS AND DISCUSSION

We turn now to the SEMPA measurements of the patterned nanodisk sample of Fig. 2, which were carried out at room temperature under ultrahigh vacuum. The sample surface was cleaned by Ar-ion bombardment while measuring the surface composition with Auger spectroscopy. The sample was then coated with a 0.5-nm-thick Fe film to enhance the magnetic contrast. This Fe film is not thick enough to be ferromagnetic by itself on the bare Si substrate but it exchange couples to the ferromagnetic elements. In other samples we have studied, the Fe contrast layer did not alter the magnetic domain structure. The probing depth for the spin-polarized secondary electrons is $\approx$1 nm and the incident electron probe diameter is $\approx$10 nm. The sample was left in the as-grown magnetic state and no external magnetic fields were applied. All of the SEMPA measurements were of this remanent state.

The results of all of the SEMPA measurements are summarized in Fig. 4. From the array shown in Fig. 2 we focused on four diameters and nine thicknesses that sample the interesting parts of the phase diagram near the phase boundaries
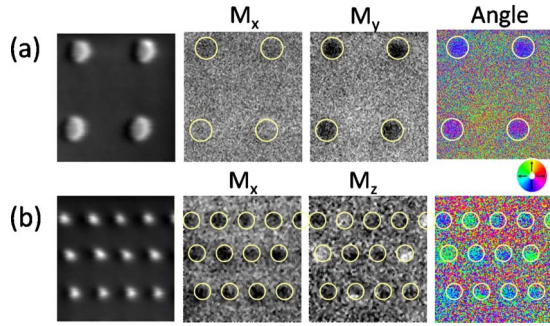
FIG. 5. (Color online) SEMPA images of (a) in-plane magnetic states in 90 nm diameter ×10-nm-thick disks and (b) out-of-plane magnetic states in 35 nm diameter ×65-nm-thick disks. Simultaneously measured topography and either two in-plane, or one in-plane and the out-of-plane magnetization components are shown. From these components, (a) the in-plane magnetization angle and (b) the out-of-plane magnetization tilt angle in the M_x and M_z plane were derived. Note that the out-of-plane magnetic structure has a significant in-plane component which may indicate curling of magnetization near the top surface.

and the triple point. The dashed lines show the phase boundaries obtained from a micromagnetic simulation to be discussed below. The next four figures illustrate the type of data going into the compilation of Fig. 4 including data from some particularly interesting regions of the phase diagram.

The SEMPA magnetization images of Fig. 5 show examples of two of the magnetic ground states, and clearly demonstrate the striking dependence of the magnetic nanostructure on the nanodisk aspect ratio. Figure 5 shows the SEMPA images of (a) low aspect ratio (90 nm in diameter ×10 nm in thickness) nanodisks with in-plane magnetization and (b) high aspect ratio (35 nm in diameter ×65 nm in thickness) disks (or pillars) with out-of-plane magnetization. The images correspond to the extreme lower right and upper left points, respectively, in Fig. 4. The images in the first column of Fig. 5 are intensity, and the images in the second and third columns are the corresponding magnetization contrasts measured simultaneously. For in-plane magnetization measurement, by combining the M_x and M_y images, we obtain the direction of the in-plane magnetization or angle, $\theta_{xy} = \tan^{-1}(M_y/M_x)$. Figure 5(a) shows weak M_x contrast and strong M_y contrast, and the combined angle image is represented in color with directions given by a color wheel. The calculated value for the surface magnetization direction is 228° ±5° (Ref. 33) (0° points to the right). Note that an independent measurement of M_z on these disks did not show any magnetic contrast. However, the nanodisks with high aspect ratio, that is, nanopillars, show either bright or dark out-of-plane magnetization as in the M_z image of Fig. 5(b). Surprisingly, the magnetization in the surface region measured by SEMPA also has a significant in-plane, M_x, component as well as an out-of-plane, M_z, component. This corresponds to a surface magnetization that is tilted into or out of plane by 30° ±10° with respect to the surface. The color wheel for Fig. 5(b) corresponds to $\theta_{xz} = \tan^{-1}(M_z/M_x)$. We speculate that the observed in-plane magnetization component may be due to tilting of the surface magnetization in order to reduce the magnetostatic energy at the top surface.
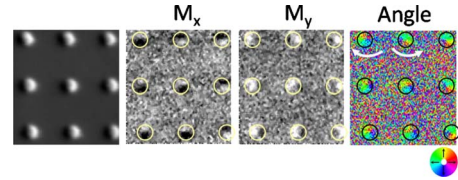

FIG. 6. (Color online) SEMPA images of vortex magnetic states in 90 nm diameter ×35-nm-thick disks. The in-plane magnetization direction is represented by the inset color wheel. The array contains vortex states with two different chiralities.

The resulting magnetic configuration would be an out-of-plane state with curling of magnetization near the top surface. This is reminiscent of an asymmetric surface Néel wall cap on an interior Bloch wall which minimizes the surface magnetostatic energy in the bulk sample.[34]

The SEMPA magnetization images of Fig. 6 for nanodisks with a diameter of 90 nm and a thickness of 35 nm present a clear example of the third nanodisk magnetic ground state, a vortex state. The M_x and M_y components have both dark and bright regions present within each nanodisk, which is characteristic of a magnetic vortex state. Furthermore, from the derived in-plane magnetization angle image shown in Fig. 6 one can see that both of the two possible chiralities of magnetic vortex are present in this nanodisk array. We did not attempt to measure the vortex core polarity for these nanodisks.

Near the phase boundaries and the triple point, it is not unusual to find multiple different phases present simultaneously. The series of the SEMPA images in Fig. 7 shows the transition from the vortex phase to the in-plane phase, and the mixture of the two ground-state phases near the phase boundary, for 65 nm diameter nanodisks as the thickness decreases from (a) 48 nm, (b) 35 nm, to (c) 20 nm. In Fig. 7(a), all the nanodisks show dark/bright contrast indicating vortex magnetization. However, in Fig. 7(b), the nanodisks in the first row show uniform contrast while the rest of the nanodisks in the array show dark/bright contrast. This indicates a mixture of the in-plane state and the vortex state in the 65 nm in diameter ×35 nm in thickness nanodisk array. In Fig. 7(c), all the nanodisks but the one at the bottom left corner show uniform brightness representing the in-plane state. We note that the simultaneous measurements of the M_z component in these disks have no magnetic contrast (not shown).
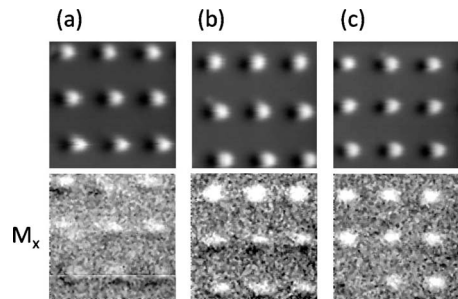

FIG. 7. SEMPA images which show the transition with decreasing thickness from a vortex state in (a) to an in-plane state in (c). Disk thicknesses were (a) 48 nm thick, (b) 35 nm thick, and (c) 20 nm thick. Disk diameters were all 65 nm. In (b), a mixture of the two ground phases is observed near phase boundary.
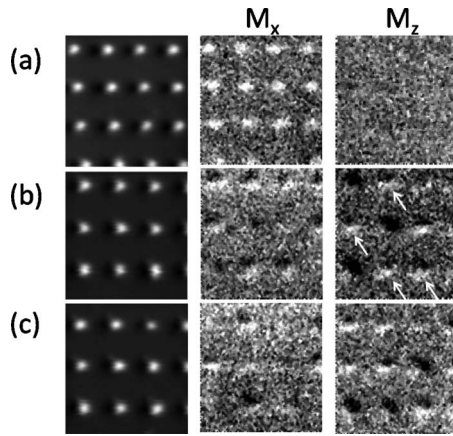
FIG. 8. SEMPA images of disks with sizes along the out-of-plane/vortex phase boundary. Disk thicknesses were (a) 35 nm, (b) 48 nm, and (c) 65 nm. Disk diameters were all 45 nm. In addition to showing the transition from (a) in-plane state to (c) out-of-plane state with increasing thickness, the images also reveal more complex magnetic states such as the tilted vortex states indicated by arrows in (b).

Figure 8 shows a series of the SEMPA images of permalloy nanodisks with the same 45 nm diameter near the out-of-plane-to-vortex phase boundary. This slice through the phase diagram is interesting both for the presence of multiple states near the phase boundary, and the existence of complex states that are some combination of the three basic magnetic phases. The images of nanodisks, which are (a) 35 nm thick, (b) 48 nm thick, and (c) 65 nm thick, show the transition from the in-plane state to complex out-of-plane states with increasing thickness. For thin nanodisks the surface magnetization is in-plane [Fig. 8(a)] whereas images of the thick nanodisks show stronger out-of-plane magnetization contrast [Fig. 8(c)]. However, in the intermediate case [Fig. 8(b)], the nanodisks have uniform or dark/bright contrast in both M_x and M_z components. Interestingly, some nanodisks have dark/bright contrast for both in-plane and out-of-plane magnetization [see arrows in Fig. 8(b)]. While the dark/bright contrast in the in-plane component indicates a vortex state, the dark/bright contrast in the out of plane component is consistent with a vortex that is tipped with respect to the surface plane. Thus in this crossover region of the phase diagram we observe a *tilted* vortex magnetization state that is a magnetization configuration intermediate between the three ground-state phases. The tilting angle determined from M_x and M_z values in areas of maximum contrast is $55° \pm 7°$ with respect to the surface plane. Near the triple point, the SEMPA measurement also showed the coexistence of different ground phases and complex tilted phases but some nanodisks did not have significant magnetic contrast in either M_x or M_z components making them difficult to interpret.

The magnetic ground states of isolated $Ni_{80}Fe_{15}Mo_5$ nanodisks with different geometries were calculated using the OOMMF micromagnetic simulation code with edge corrections.[35,36] The material parameters used were the saturation magnetization $M_s = 8.0 \times 10^5$ A/m and the exchange stiffness $A = 1.3 \times 10^{-11}$ J/m. The crystalline anisotropy was neglected. The unit-cell size for the three-dimensional simu-

lation was 1 nm $\times$ 1 nm $\times$ 1 nm, which is much smaller than the exchange length $l_{ex} \approx 5.7$ nm. The magnetic behavior of a $Ni_{80}Fe_{15}Mo_5$ nanodisk is closely related to the magnetic exchange length, which in turn can be used to scale the geometric dimensions in the phase diagram.

Micromagnetic calculations were carried out using different initial states. For each nanodisk geometry, separate energy minimizations were carried out starting from vortexlike, in-planelike, and out-of-planelike initial states. In each case, the initial states were made slightly asymmetric to ensure that the resulting states were stable. From these equilibrium states, the ground-state phase diagram was determined by selecting the state with the smallest energy. The bistable regions of the phase diagram were determined by noting which sample dimensions resulted in more than one equilibrium state.

Figure 9(a) shows the magnetic ground-state phase diagram of $Ni_{80}Fe_{15}Mo_5$ nanodisks as a function of the disk diameter and thickness derived from the micromagnetic model. The phase diagram shows the three phases (the in-plane, the out-of-plane, and the vortex state) and the approximate phase boundaries. The different phases are represented by the out-of-plane (M_z) component of magnetization in the plot. The in-plane phase has $M_z \approx 0$ and the out-of-plane phase has $M_z \approx 1$. The vortex phase shows decreasing M_z with increasing diameter. The triple point of the three phases is also shown at the diameter of ≈ 40 nm and the thickness of ≈ 35 nm. In terms of M_z, the transition from the in-plane state to the out-of-plane state or from the in-plane state to the vortex state is discontinuous. In particular, the phase boundary between the in-plane and the out-of-plane states is close to the aspect ratio of ≈ 0.9, which is in good agreement with the analytical calculation by assuming the uniform demagnetization factor[21] and quasiuniform magnetization state.[37] In contrast, M_z varies continuously in the transition from the out-of-plane state to the vortex state, with an abrupt change in the slope of M_z vs diameter at the phase boundary. Moving away from this phase boundary with increasing diameter, the vortex state develops from the out-of-plane state as the magnetization around the circumference of the disk twists and tilts toward the in-plane direction leaving vertically oriented magnetization in the vortex core.

Regions of bistability, where the magnetic ground-state phase along with one or more metastable states might coexist, are shown in Fig. 9(b). In the micromagnetic simulations bistable regions occur near the in-plane to vortex phase boundary and near the in-plane to out-of-plane phase boundary. No bistability was found near the out-of-plane to vortex phase boundary. Bistability in the model is only observed at phase boundaries where the magnetization pattern changes discontinuously.

The existence of metastable states near the phase boundary was also described recently by an analytical calculation.[22] It is interesting to compare the results of that calculation with the results of our micromagnetic model and our SEMPA measurements. Both models agree on the location of the triple point, the out-of-plane to in-plane phase boundary and the out-of-plane to vortex boundary. Compared to the analytical calculation, the vortex to in-plane phase transition occurs at larger thicknesses in our micromagnetic
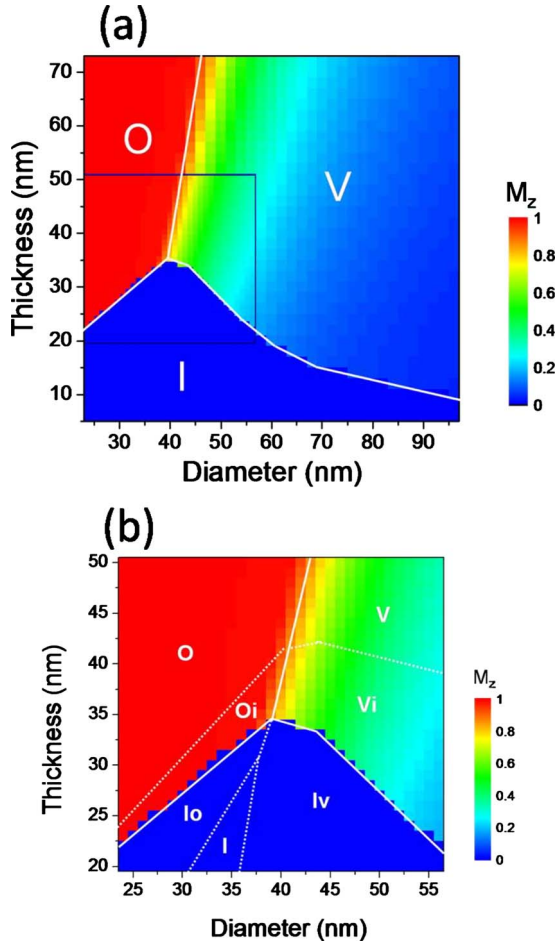
FIG. 9. (Color online) Nanodisk magnetic state phase diagrams derived from OOMMF micromagnetic simulations. The phase diagrams show the boundaries between the three basic phases (in-plane: **I**, out-of-plane: **O**, and vortex phase: **V**), and the color-coded, normalized out-of-plane magnetization component (M_z). (a) Main phase boundaries (solid lines) between minimum-energy ground states. (b) Metastable phase boundaries (dashed lines) near the triple point [boxed region in (a)] that arise when more than one stable state was found. In the metastable regions the capital letters correspond to the magnetic ground phase while the small letters represent metastable phases.

model and in our SEMPA measurements but the phase boundary has the same functional shape. The largest differences between models and data occur in the metastable regions of the phase diagram. For example, while our micromagnetic model does not predict the existence of metastable states along the vortex to out-of-plane phase boundary, the analytical model does.

The existence of metastable states along phase boundaries can partly explain the mixture of ground states near the phase boundaries and triple point that were observed by SEMPA. Multiple stable states in larger disks along the vortex to in-plane phase boundary have also been observed in magneto-optic measurements of nanodisk arrays[38] and spin-polarized low-energy electron microscopy of isolated Co nanodots.[39] However, while the model calculations can iden-

tify regions where metastable states may exist, other extrinsic individual nanodisk properties may effect the probability of finding a nanodisk in a particular state at remanence. Specifically, in those regions near the phase boundaries, we speculate that the stable states of each individual nanodisk may depend more strongly on the small variations in the nanodisk geometry, grains, defects, and surface and edge roughness than in the regions far from the phase boundaries.

The SEMPA measurements also revealed states that were not predicted from the micromagnetic calculations. Neither the in-plane surface magnetization of the out-of-plane state shown in Fig. 5(b) nor the tilted vortex state shown in Fig. 8(b) were observed in the micromagnetic calculations. Initial states mimicking a tilted uniform state or a tilted vortex state proved to be unstable in the cylinder geometry. These unexpected magnetic states may be due to deviations from the ideal cylindrical geometry, and should therefore be most likely for the smallest, and therefore most lithographically challenging disk shapes. However, stable tilted vortex states have been calculated in a cubic geometry.[40]

IV. CONCLUSIONS

In conclusion we have measured the $Ni_{80}Fe_{15}Mo_5$ nanodisk magnetic state phase diagram by using SEMPA to directly image the in-plane and out-of-plane magnetic structure of individual nanodisks with different diameters and thicknesses. We determined the phase boundaries and the triple point between the three basic magnetic states: in-plane, out-of-plane, and vortex. While this basic phase diagram is similar to ones determined by earlier measurements, we find the phase diagram is more complex. Specifically, near the phase boundaries and the triple point, multiple ground states or complex metastable states are observed at remanence in nanodisks with nominally identical dimensions. Note that these states would have been very difficult to identify from nonspatially resolved measurements of average magnetic properties of the disk arrays. The phase diagram determined by the SEMPA measurements agrees qualitatively with the magnetic phase diagram computed from our OOMMF micromagnetic simulations and with an analytical model.[22] However, we observed a few structures, such as tilted vortex states, that were not predicted by the modeling, possibly due to deviations from ideal geometries. Finally, we note that by scaling the results using appropriate exchange lengths, these measurements of nanodisk magnetic phases in the sub-100 nm regime can also be applied to determining the magnetic phases for nanostructures with different materials and magnetic properties. This result will enable tailoring material properties and the geometry of nanostructures for various potential applications.

ACKNOWLEDGMENTS

[1] S. A. Wolf, A. Y. Chtchelkanova, and D. M. Treger, IBM J. Res. Dev. **50**, 101 (2006).

[2] S. Y. Chou, Proc. IEEE **85**, 652 (1997).

[3] S. Parkin, J. Xin, C. Kaiser, A. Panchula, K. Roche, and M. Samant, Proc. IEEE **91**, 661 (2003).

[4] D. C. Ralph and M. D. Stiles, J. Magn. Magn. Mater. **320**, 1190 (2008).

[5] E. Feldtkeller and H. Thomas, Phys. Kondens. Mater. **4**, 8 (1965).

[6] A. Hubert and R. Schafer, *Magnetic Domains: The Analysis of Magnetic Microstructures* (Springer, Berlin, 1998).

[7] J. K. Ha, R. Hertel, and J. Kirschner, Phys. Rev. B **67**, 224432 (2003).

[8] C. A. Ross, M. Hwang, M. Shima, J. Y. Cheng, M. Farhoud, T. A. Savas, H. I. Smith, W. Schwarzacher, F. M. Ross, M. Redjdal, and F. B. Humphrey, Phys. Rev. B **65**, 144417 (2002).

[9] K. Y. Guslienko, V. Novosad, Y. Otani, H. Shima, and K. Fukamichi, Phys. Rev. B **65**, 024414 (2001).

[10] S.-B. Choe, Y. Acremann, A. Scholl, A. Bauer, A. Doran, J. Stohr, and H. A. Padmore, Science **304**, 420 (2004).

[11] R. P. Cowburn and M. E. Welland, Science **287**, 1466 (2000).

[12] B. Van Waeyenberge, A. Puzic, H. Stoll, K. W. Chou, T. Tyliszczak, R. Hertel, M. Fähnle, H. Brückl, K. Rott, G. Reiss, I. Neudecker, D. Weiss, C. H. Back, and G. Schütz, Nature (London) **444**, 461 (2006).

[13] K. Yamada, S. Kasai, Y. Nakatani, K. Kobayashi, H. Kohno, A. Thiaville, and T. Ono, Nature Mater. **6**, 270 (2007).

[14] W. F. Brown, *Micromagnetics* (Wiley, New York, 1963).

[15] W. Scholz, K. Yu. Guslienko, V. Novosad, D. Suess, T. Schrefl, R. W. Chantrell, and J. Fidler, J. Magn. Magn. Mater. **266**, 155 (2003).

[16] K. L. Metlov and K. Yu. Guslienko, J. Magn. Magn. Mater. **242-245**, 1015 (2002).

[17] P. O. Jubert and R. Allenspach, Phys. Rev. B **70**, 144402 (2004).

[18] J. Mejia-Lopez, D. Altbir, A. H. Romero, X. Batlle, I. V. Roshchin, C. Li, and I. K. Schuller, J. Appl. Phys. **100**, 104319 (2006).

[19] P. Landeros, J. Escrig, D. Altbir, D. Laroze, J. d'Albuquerque e Castro, and P. Vargas, Phys. Rev. B **71**, 094435 (2005).

[20] J. d'Albuquerque e Castro, D. Altbir, J. C. Retamal, and P. Vargas, Phys. Rev. Lett. **88**, 237202 (2002).

[21] A. Aharoni, J. Appl. Phys. **68**, 2892 (1990).

[22] K. L. Metlov and Y. P. Lee, Appl. Phys. Lett. **92**, 112506 (2008).

[23] C. A. Ross, M. Farhoud, M. Hwang, H. I. Smith, M. Redjdal, and F. B. Humphrey, J. Appl. Phys. **89**, 1310 (2001).

[24] R. P. Cowburn, D. K. Koltsov, A. O. Adeyeye, M. E. Welland, and D. M. Tricker, Phys. Rev. Lett. **83**, 1042 (1999).

[25] I. L. Prejbeanu, M. Natali, L. D. Buda, U. Ebels, A. Lebib, Y. Chen, and K. Ounadjela, J. Appl. Phys. **91**, 7343 (2002).

[26] G. D. Skidmore, A. Kunz, C. E. Campbell, and E. D. Dahlberg, Phys. Rev. B **70**, 012410 (2004).

[27] J. N. Chapman, P. R. Aitchison, K. J. Kirk, S. Mcvitie, J. C. S. Kools, and M. F. Gillies, J. Appl. Phys. **83**, 5321 (1998).

[28] M. Huber, J. Zweck, and D. Weiss, Phys. Rev. B **77**, 054407 (2008).

[29] M. Schneider, H. Hoffmann, and J. Zweck, Appl. Phys. Lett. **77**, 2909 (2000).

[30] R. M. Bozorth, *Ferromagnetism* (D. Van Nostrand, New York, 1951).

[31] M. R. Scheinfein, J. Unguris, M. H. Kelley, D. T. Pierce, and R. J. Cellota, Rev. Sci. Instrum. **61**, 2501 (1990).

[32] J. Unguris, in *Experimental Methods in the Physical Sciences*, edited by M. De Graef and Y. Zhu (Academic, New York, 2001), Vol. 36, pp. 167–194.

[33] Unless otherwise noted, all uncertainty estimates in this paper are intended to be interpreted as one-standard deviation combined standard uncertainty.

[34] M. R. Scheinfein, J. Unguris, R. J. Celotta, and D. T. Pierce, Phys. Rev. Lett. **63**, 668 (1989).

[35] M. J. Donahue and D. G. Porter, National Institute of Standards and Technology, Interagency Report No. NISTIR 6376, 1999 .

[36] M. J. Donahue and R. D. McMichael, IEEE Trans. Magn. **43**, 2878 (2007).

[37] K. L. Metlov and K. Yu. Guslienko, Phys. Rev. B **70**, 052406 (2004).

[38] A. V. Jausovec, G. Xiong, and R. P. Cowburn, J. Appl. Phys. **99**, 08B103 (2006).

[39] H. F. Ding, A. K. Schmid, D. Li, K. Yu. Guslienko, and S. D. Bader, Phys. Rev. Lett. **94**, 157202 (2005).

[40] M. J. Donahue (private communication).